Title
Observing Conductive Properties of Ionogel Electrolytes for Solid State Batteries

Author
White, Makena

Publication Date
2021

Peer reviewed|Thesis/dissertation

UNIVERSITY OF CALIFORNIA

Los Angeles

Observing Conductive Properties of Ionogel Electrolytes for Solid State Batteries

A thesis submitted in partial satisfaction

of the requirements for the degree Master of Science

in Materials Science and Engineering

by

Makena White

2021

ABSTRACT OF THE THESIS

Observing Conductive Properties of Ionogel Electrolytes

for Solid State Batteries

by

Makena White

Master of Science in Materials Science and Engineering

University of California, Los Angeles, 2021

Professor Bruce S. Dunn, Chair

Increased demand for battery power due to technological advancement requires more efficient, safer battery systems to be developed. Ionogels, which confine liquid electrolyte interspersed in a nanoporous inorganic matrix, have generated interest due to their ionic conductivity, stability, and capability of providing a solid structure while allowing liquid behavior at the nanoscale. Herein, the results for impedance and microstructure data are reported for ionogels that were processed with varying volumetric amounts of ionic liquid electrolyte (ILE). The gels were created using a standard gelation method, and their conductivities were on the same order of magnitude as the neat ILE. While their room-temperature conductivity was half of the neat ILE at 0.282 mS/cm, the conductivity closed the gap to 70 percent of the ILE at 10.6 mS/cm at 80 ºC. The activation energy of the most conductive sample, 0.25 eV, is not much higher than

the neat ILE at 0.2 eV. The microstructure data obtained using BET and BJH was in agreement with the reference for a simpler ionogel, but the large pore size of the tested samples was too large to obtain an accurate average pore size. The quantity adsorbed for the current work was also less than a third of the reference, which also indicates its larger pore structure.

The thesis of Makena White is approved.

Qibing Pei

Aaswath Pattabhi Raman

Bruce S. Dunn, Committee Chair

University of California, Los Angeles

2021

Table of Contents

List of Figures

List of Tables

1. Background

1a. Battery Importance in Society

Batteries play an integral role in the energy industry because of their versatility for electrical systems support. They provide a mobile source of energy for innumerable types of devices and can even serve as backup for power generation systems. A fairly saturated market for batteries is consumer electronics and devices, while growing markets are grid energy/industry and transportation [1]. To develop with these growing markets, battery performance must keep up with the demand. This is expected to exponentially increase, as showing in Figure 1.1 [1], so batteries must be more energy dense and more efficient to fulfill this need.

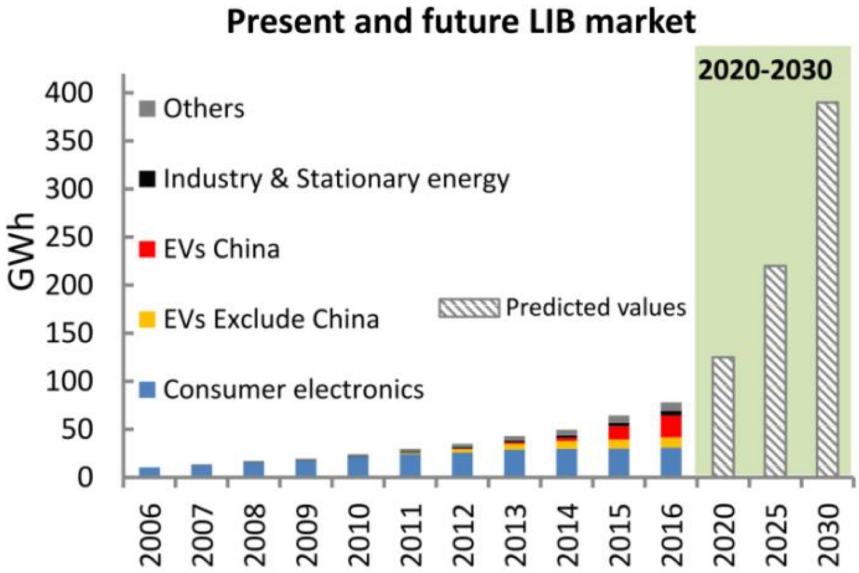

Figure 1.1: Projected demand for battery power.

1b. Basics of Battery Systems

When a battery is charged, electrons flow from the cathode (positive electrode) to the anode (negative electrode) via an external system. Positively charged ions travel in the same direction

through the battery electrolyte. Discharging the battery reverses the flow of electrons and allows for the recombination of ions and electrons in each side of the battery, as shown in Figure 1.2 [2].

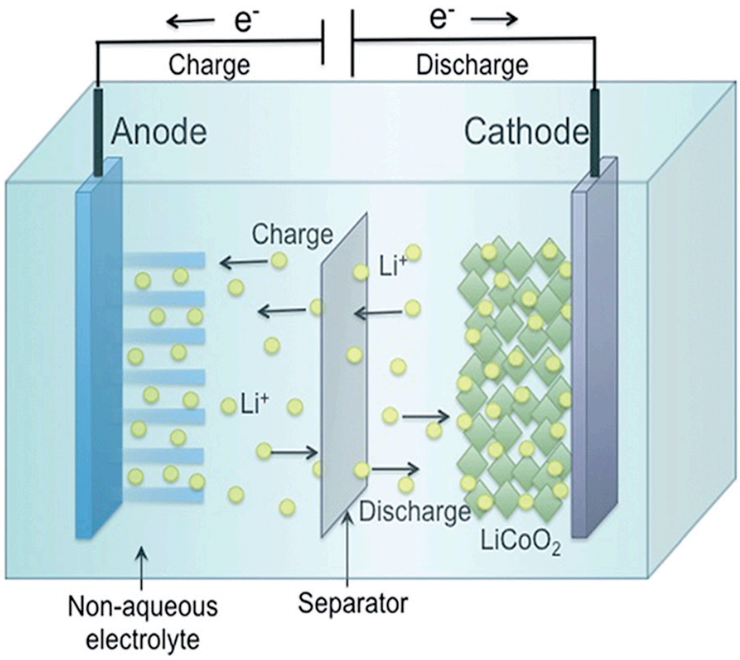

Figure 1.2: Schematic of electron and ion flow during charge and discharge of a battery.

The following reactions occur during charging [3], specifically for the $LiCoO_2$-graphite cathode-anode system in Figure 1.2:

$$\text{Cathode:} \quad 6C + xLi^+ + xe^- \rightarrow C_6Li_x$$

$$\text{Anode:} \quad LiCoO_2 \rightarrow L_{(1-x)}CoO_2 + xLi^+ + xe^-$$

The opposite reactions occur during discharge. This is called a reduction-oxidation (redox) reaction, which is the driving force behind generating electrical energy from a battery system [4]. The cathode is the oxidant and the anode is the reductant, and the difference in chemical potentials of the two electrodes is because of the concentration gradient of lithium [5]. When oxidation occurs in the cathode during charging, the removal of ions and electrons reduces its chemical potential, while when reduction occurs in the anode the insertion of ions and electrons increases its chemical potential. This effective potential, or voltage, change is related to the energy stored in the battery;

the energy is simply the magnitude of transferred charge (e) multiplied by the voltage change (V) or the chemical potential difference between the cathode and anode [5]:

$$E = e * V = \mu_A - \mu_C$$

Many combinations of cathodes and anodes are possible, and a specific setup is decided for its desired electrochemical potential, stability, and cost [6]. For intercalation cathodes, in which the Li^+ ions can be stored in the network and removed without damaging the structure, transition metal oxides are the most widely studied type of cathode [6]. Polyanion compounds are another type of intercalation cathode, in which polyanions with generic formula $(XO_4)^{3-}$ occupy lattice sites and increase redox potential while stabilizing the structure. Other types of cathodes include conversion cathodes, which reversibly change their crystalline structure during the redox reactions by breaking and recombining chemical bonds [6]. Table 1.1 displays some examples of cathodes [6].

Table 1.1: Characteristics of Representative Cathode Compounds

Crystal Structure	**Compound**	**Theoretical Specific Capacity (mAh/g)**	**Theoretical Volumetric Capacity (mAh/cm^3)**	**Average Voltage (V)**
Layered	$LiCoO_2$ (LCO)	274	1363	1.9
	$LiNi_{0.33}Mn_{0.33}Co_{0.33}O_2$ (NMC)	280	1333	3.7
	$LiNi_{0.8}Co_{0.15}Al_{0.05}O_2$ (NCA)	279	1284	3.7
Spinel	$LiMn_2O_4$ (LMO)	148	596	4.1
Olivine	$LiFePO_4$ (LFP)	179	589	3.4

LCO was the first commercially successful layered transition metal oxide cathode, but its high cost and instability due to its cobalt content prompted the discovery of other cheaper, safer options [6]. NMC and NCA are suitable alternatives; they reduce the amount of cobalt with cheaper alternatives like nickel, manganese, and aluminum without sacrificing capacity. LMO is even

cheaper than NMC or NCA because manganese is more available, but these cathodes are not suitable long-term due to Mn leaking out of the cathode during cycling [6]. LFP is known for its high thermal stability, but its average voltage is lower than other options.

For anodes, ideal properties are maximum ion insertion and a small volume change during intercalation. Anode classification also is split into intercalation and conversion materials, and intercalation anodes are also more effective and appear in more commercial products [6]. Table 1.2 contains information about some studied anodes [6][7].

Table 1.2: Characteristics of Representative Anode Compounds

Material	**Theoretical Specific Capacity (mAh/g)**	**Theoretical Volumetric Capacity (mAh/cm^3)**	**Average Voltage (V)**	**Volume Change (%)**
Graphite	372	380	0.07	10
$Li_4Ti_5O_{12}$ (LTO)	175	600	1.55	0.20
Si	4012	9340	0.05	270
Sn	959	7000	0.4	255

Graphite is the most commonly used anode due to its availability and high electrical conductivity [6], but its capacity leaves something to be desired. While Si and Sn have much higher specific and volumetric capacities, their volume change of over 250% causes internal stresses in the anode. This degrades the material quickly and thus is not suitable for a battery that must be stable [6]. Conversely, LTO's volume change is 0.20% but its average voltage reduces the chemical potential between the anode and the cathode and therefore the amount of energy that can be stored in the battery.

For electrolytes, it is beneficial if the chemical potentials of the electrodes reside within the voltage window of the electrolyte [5]. Electrolytes must also have a high lithium transference number close to 1, so ions are not lost to side reactions during cycling, low toxicity, and nonflammable in the case of a short-circuit [5]. Commercial batteries contain liquid electrolyte

due to its superior wetting to active materials and faster charge transport [8]. They are normally synthesized by dissolving salts in either aqueous or nonaqueous polar solvents. Because they need to be electrochemically inert at the electrode surfaces to insulate from electronic conduction, additives passivate the surface of the electrode into a solid electrolyte interphase (SEI) [8]. The most common salt for liquid electrolytes is lithium hexafluorophosphate ($LiPF_6$) and the solvents can be combinations of organic carbonates like ethylene carbonate (EC), dimethyl carbonate (DMC), propylene carbonate (PC), diethyl carbonate (DEC) and ethyl methyl carbonate (EMC) [9]. $LiPF_6$ is ideal for nonaqueous electrolytes because its strong Lewis acid product PF_5 is highly reactive and it can support the operation of 4.0 V cathode materials, a necessity for energy-dense systems [10].

1c. Types of Solid-State Electrolytes

While the liquid electrolytes mentioned above have been successfully used for many years, there are drawbacks that include low thermal and electrochemical stability and relatively low flash points that can lead to flammability risks [11]. Two types of solid-state electrolytes under consideration for replacing liquid electrolyte are crystalline [11] and amorphous, matrix-encapsulated ionic liquid electrolytes [12].

1ci. Crystalline Solid Electrolytes

Crystalline solid-state electrolytes transport ions between Schottky and Frenkel defects in response to applied concentration gradients and electric fields [11]. In order for these electrolytes to be viable solid electrolyte materials, there must be more available sites for ion occupation than there are mobile species, low enough energy barriers for ions to easily move between sites, and an available, continuous pathway for ions to travel [11]. The NASICON-type compounds are considered to be suitable solid electrolytes for high-voltage batteries because of their high

chemical, electrochemical, and mechanical stability [11]. The general formula is $AM_2(PO_4)_3$, in which A is Li, Na, or K and M is Ge, Zr, or Ti. Conductivity ranges from 10^{-5} – 10^{-3} S/cm, on par with liquid electrolytes [11]. However, these compounds are hard to manufacture and are thus undesirable for large-scale production.

Sulfide-based systems like Li_2S—SiS_2 have also been studied due to their high lithium ion conductivity and thermal stability [11]. The highest reported conductivity is 6.9 x 10^{-4} S/cm from a Li_2S—SiS_2 system doped with Li_3PO_4 [11]. This doping with metal oxides creates a LISICON (lithium superionic conductor) crystalline material not unlike NASICON compounds. While all of these elements are easy to procure, the chemical stability of the system is poor as it is sensitive to moisture and readily generates gaseous H_2S, a flammable gas that is not desirable in a battery system.

1cii. Ionogels: An Alternative Hybrid Electrolyte

A more balanced approach to formulating electrolytes with a definable shape has led to the discovery and development of ionogels, a type of sol-gel structure that can present as a solid material but can behave microscopically as a liquid [13]. Ionogels are composed of an ionic liquid and an organic or inorganic matrix to suspend the liquid into a solid form [14]. An ionic liquid is defined as a salt that has a melting point under 370 K. They are generally salts made of organic cations like ammoniums, imidazoliums, and pyridiniums, while the anions can be PF_6^-, BF_4^-, or bis(trifluoromethanesulfonyl)imide $(TFSI)^-$ [9]. They can act as solvents for solid lithium salts to enhance their conductive properties. Ionic liquids are promising candidates for battery electrolyte formulation due to their already high ionic conductivity and wide electrochemical potential window. A list of some ionic liquids is included in Table 1.3 [15]. [EMIM] is 1-ethyl-3-methylimidazolium and [BMIM] is 1-butyl-3-methylimidazolium.

Table 1.3: Properties of Imidazolium Ionic Liquids

Ionic Liquid	Conductivity [mS/cm]	Viscosity [cP=0.1 Ns/m^2]	Electrochemical Window [V]
[EMIM][TFSI]	8.8	35	4.3
[BMIM][TFSI]	3.7	90	4.6
[EMIM][BF_4]	14	25.7	4.0
[BMIM][BF_4]	1.21	180	4.2

Normally a sol-gel is processed to remove the liquid phase, leaving behind the porous gel which is then known as an aerogel. If the liquid is allowed to evaporate out of the network with no controlling mechanisms under ambient conditions, the network will collapse and create a xerogel [13]. However, because the ionic liquid of the ionogel is beneficial for the electrochemical properties of the material, it is advantageous for it to remain inside the gel network. This is partly possible because ionic liquids have very low vapor pressure because its strong intermolecular bonds prevent molecules from escaping the solid [13]. This would not be the case for other solvents used for liquid electrolytes, which is why $LiPF_6$-based liquid electrolytes as described earlier cannot be converted into ionogels. Also, the nanoscale pore network created by the matrix keeps the ionic liquid inside the ionogel due to capillary forces trapping the ionic liquid in the pores so the liquid does not seep out. This retainment of ionic liquid allows for a material that can act as a liquid at the nanoscale but remains a macroscopically solid structure [13].

This nanopore network also affects various physical and chemical properties of the ionogel. Because of better force distribution throughout the matrix than in microsized or polymer matrices, the matrix can handle more mechanical loading than other structures and does not need to increase matrix concentration at the cost of ionic conductivity [12]. Engineering the pores shapes to hexagonal nanopores can further increase mechanical strength. The thermal stability of the ionogel is also enhanced; the physical confinement in the nanoscale matrices retards ionic liquid decomposition and raises its thermal stability by around 10 – 20 ºC [12]. Even the electrochemical

stability is improved, as the surface interactions with imidazolium ionic liquids stabilizes them at high voltages normally outside their electrochemical window [12]. While there are many benefits to this nanoscale matrix, the ionic conductivity is not always as high as the ionic liquid alone, as tortuosity effects can slow the ion transport through the electrolyte [13].

1d. Sol-Gel Synthesis Theory

The etymological breakdown of sol-gel consists of a *sol*, a stable suspension of colloidal particles in a liquid, and a *gel*, a porous, solid network supporting a continuous liquid phase [16]. The gel is formed by the transformation of alkoxo and silanol species to siloxane compounds using condensation reactions in an alkoxide-based system, usually by connecting SiO_4 tetrahedra [16].

Common precursors are aqueous silicates and silicon alkoxides. In an alkoxide-based system, a common alkoxysilane ($R'Si(OR)_3$) is triethoxyvinylsilane (VTEOS). Tetraalkoxysilanes ($Si(OR)_4$) include tetramethoxysilane (TMOS) or tetraethoxysilane (TEOS).

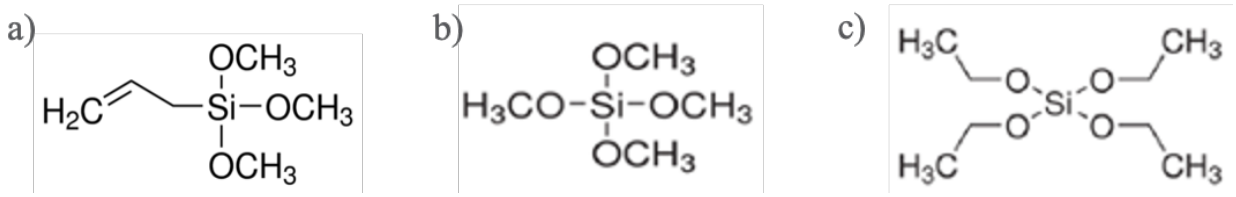

Figure 1.3: Schematic representations of VTEOS, TMOS, and TEOS.

Choosing the precursors depends on the desired properties of the final product. For example, using TMOS with VTEOS instead of TEOS will yield a denser silica structure. This is because VTEOS only has three OR groups (OCH_3 in this case) available for bonding compared to TEOS's four OR groups.

There are two main steps to gelation:

1) Hydrolysis: Si-OR groups (alkoxos) react with water to form silanol groups that are necessary for condensation [17].

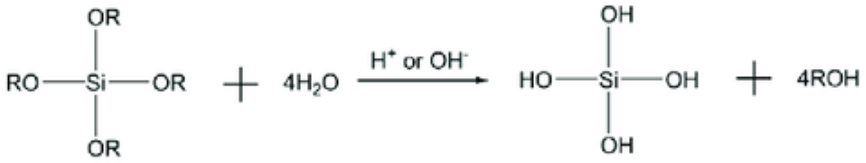

Figure 1.4: Schematic representation of the hydrolysis reaction in an alkoxide-based system.

2) Condensation: Si-O-Si (siloxane) groups form by silanol reacting with other silanol groups or with more alkoxides [17].

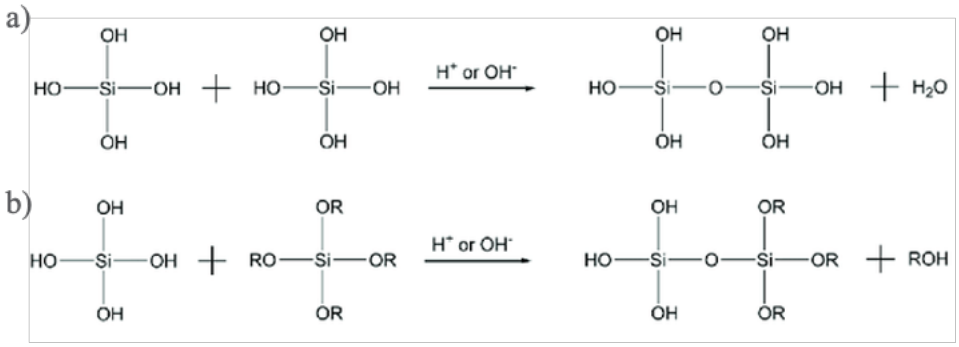

Figure 1.5: Schematic representation of the condensation reactions in an alkoxide-based system.

Figure 1.5a) represents the silanol reaction with other silanol groups, while Figure 1.5b) represents the silanol reaction with alkoxide groups. This is quite a complicated process, because reactions for hydrolysis are occurring at the same time as condensation reactions and condensation can remove reactants for hydrolysis. Therefore, it is beneficial to catalyze hydrolysis so there is enough silanol to perform condensation. Reactions with alkoxides and water are slow, so an acidic catalyst like formic acid (FA) is normally used [16]. In addition to being used as a catalyst, formic acid lowers the pH of the gel precursors, which is a significant determining factor for the gelation process [13]. The point of zero charge (PZC) is the pH at which the siliceous species is neutral and where the relative reaction rates of condensation and hydrolysis meet [16]. The relationship between the reaction rates is shown in Figure 1.6 [18].

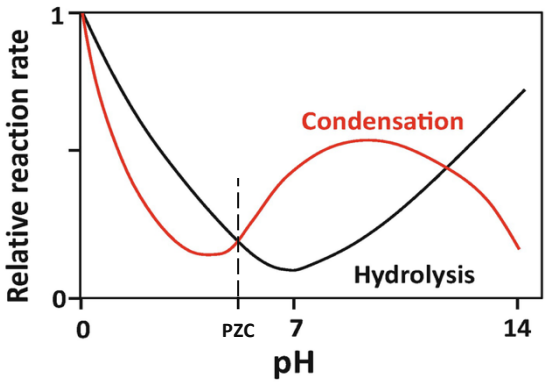

Figure 1.6: Graph of pH vs relative reaction rates.

The pH of the solution during gelation determines the outcome of the final gel. It is preferable to be above or below the PZC. If the pH of the system is at the PZC, hydrolysis and condensation compete with each other during gelation and makes it more difficult to control the structure. Below the PZC, hydrolysis is faster than condensation. Condensation in this case forms extended linear-like chains, forming an open, highly-branched network [13].

1e. Benefits of Solid-State Batteries: Using Li Metal as an Anode

Lithium metal as an anode for has been a material of interest for decades, but there are issues with long-term usage that have prevented its use in most commercial batteries. Lithium is seen as an ideal anode because of its very high theoretical capacity of 3860 mAh/g, low density of 0.59 g/cm^3, and lowest negative electrochemical potential compared to other anode materials [19]. However, its high reactivity means that it reacts with other components of the battery that cause side reactions and the formation of a solid-electrolyte interface (SEI) [19]. The SEI is made of oxides and polymeric materials that inhibit ion transfer and potency of the metal anode. Another issue is its high likelihood to instigate dendrite formation and growth. Dendrites form when there is an ion concentration potential on the surface of an electrode that is favorable for an agglomeration of ions to form [19]. This creates the start of a dendrite, and once this bump is formed it is more thermodynamically favorable for ions to build upon the dendrite than the flat

surface of the electrode [19]. Many studies of the prevalence of dendrites in lithium-metal systems have suggested that uneven electrodeposition causes these concentration potentials to form, so better deposition techniques could reduce dendrite formations [19]. Figure 1.7 demonstrates Li metal's superior weight and volumetric density to other battery technologies [20].

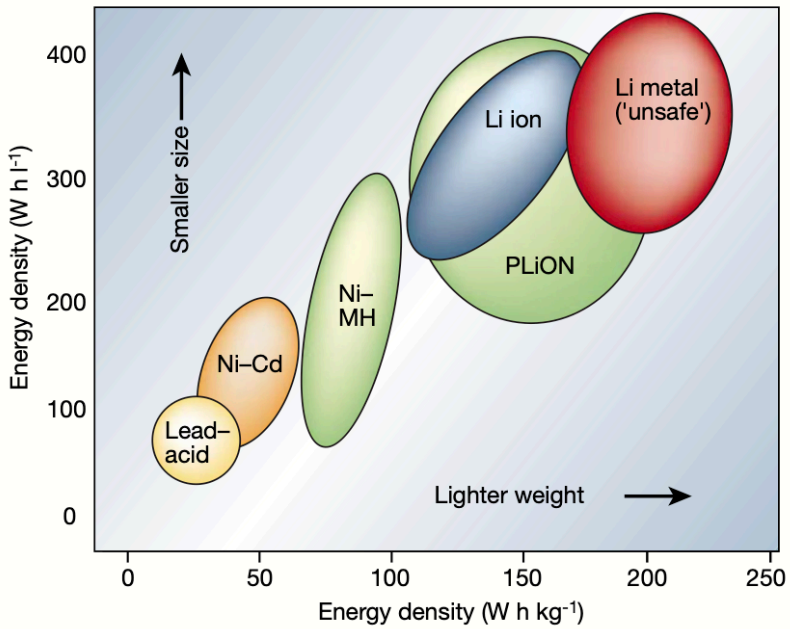

Figure 1.7: Energy density graph comparing Li metal to other battery technologies.

Fortunately, the development of solid electrolytes has allowed lithium metal to be considered again as a successful anode. In the 1970s, Sanyo Corporation developed a Li/MnO_2 battery to use in calculators, and in the 1980s the first metal lithium secondary battery Li/MoS_2 was developed for use in mobile phones [19]. However, several serious fire accidents were reported in the mobile phones, so all were recalled and research on Li-metal batteries was suspended. They were replaced by lithium-ion batteries, which used a "rocking-chair" technology that allowed for intercalation of lithium ions into the electrodes instead of using lithium metal. Graphite was the most popular anode used, and research was turned to high-voltage cathodes that compensated for graphite's higher redox potential [19]. The energy density of lithium was traded in for the safety of the Li-

ion batteries. However, now that solid-state electrolytes have piqued more interest, it is now more feasible to use Li-metal systems. The solid electrolyte, in place of a liquid electrolyte, serves as a barrier for dendrite growth. Since it is not possible for dendrites to pierce the solid electrolyte and make contact with the counter electrode, this cause of thermal runaway is eliminated.

2. Research Objectives

The research for this Master's thesis is based on two papers that concentrate on Li-based ionogels for battery applications. The first, by Néouze et. al. in 2005, is an earlier attempt at creating ionogels that trap ionic liquid in a thermally stable inorganic matrix [21]. The precursors for their ionogel are TMOS, FA, and [BMIM][TFSI] in a 1 : 7.8: 0.5 molar ratio. Gels were formed in about 1.5 hours and were aged for a few days at room temperature into transparent pellets and rods. This work was used as a reference for BET data replication; it served as a confirmation that the process for preparing BET samples was accurate.

The second paper is by Ashby et. al. in 2017, a previous graduate student of the Dunn lab [13]. This paper details the results of a standard, spin-coated ionogel film and another photo-patternable ionogel. Gel 1, the basis of this Master's thesis, is a gel that uses traditional hydrolysis and condensation with a formic acid catalyst. Gel 2 uses UV-crosslinking to create a silica structure in combination with a HPF_6 catalyst. This allows for the creation of simple structures via photolithography. Gel 1 is composed of TMOS : VTEOS : FA : 0.5 M Li:TFSI [BMIM][TFSI] ionic liquid electrolyte : cyclohexane in a 1.4 : 1 : 5.6 : 2.1 : 2.1 mole ratio or a 1 : 1 : 1 : 3 : 1 volumetric ratio. The average pore diameter was 20 nm and the surface area was 1300 m^2/g.

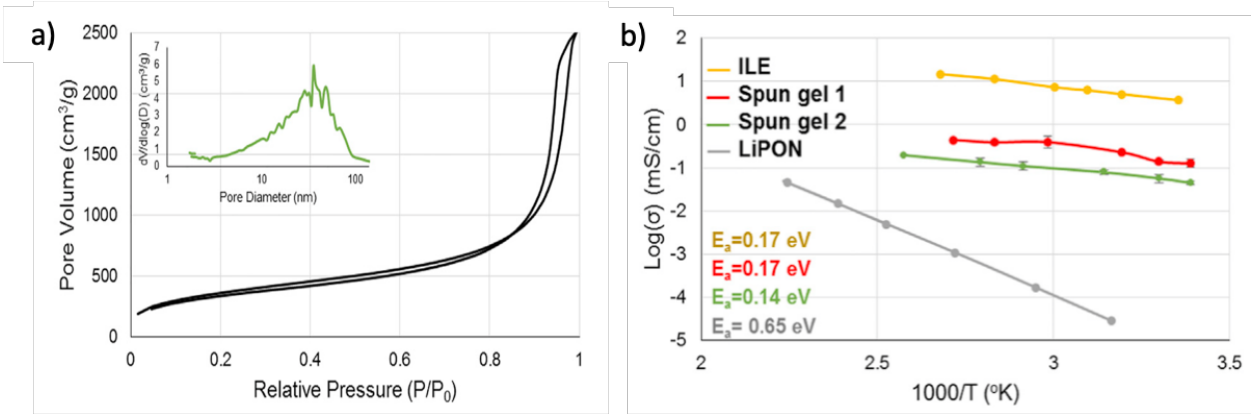

Figure 2.1: Microstructure and conductivity data from Ashby et. al.

Using the groundwork by Ashby et. al, the goal of this research project was to modify the ILE volume during synthesis and observe impedance effects. This was an exploratory research effort to better understand the synthesis and characteristics of the ionogels and how the ILE volume affects conductivity over a temperature range. The Néouze work will serve as a comparison for BET analysis, and the formulation for Gel 1 in the Ashby work will be the basis for the ionogel synthesis. One possible outcome from this work is that there may be a new formulation that performs better than the previous composition.

3. Materials and Methods

The synthesis process was adapted from Ashby et. al [13]. The ILE was 0.5 M LiTFSI [BMIM][TFSI]. 143.5 mg of LiTFSI per 1 mL of [BMIM][TFSI] was mixed inside an Ar-filled glove box overnight, then degassed at 150 °C overnight, and then stored either in a sealed container in ambient conditions or in a glove box. Water does not affect the reactions for [BMIM][TFSI], so it is stable in air [9]. In a fume hood, TMOS, VTEOS, and formic acid (FA) were combined as equal volumetric amounts, normally 100 µL each. After mixing for an hour, 250 µL, 300 µL, or 350 µL ILE and 100 µL cyclohexane were added for a total volumetric ratio of 1:1:1:x:1. The ratio of ILE was varied and was 2.5, 3, and 3.5. These samples will later be named as 250 µL, 300 µL,

and 350 µL in accordance with the amount of ILE added. Cyclohexane was necessary in the previous work as a miscible agent to aid in spin-coating; while this process was not used for this work, the cyclohexane was kept in the synthesis for consistency. The gels were left to set overnight in a fume hood inside a small plastic tube and were heated in an 80 ºC oven for another day to evaporate any solvents left in the gel.

4. Impedance Measurement and Analysis

4a. Impedance Background

Electrochemical impedance spectroscopy is a characterization method used for determining ionic conduction capabilities. It involves fitting the current response to an AC voltage sweep to fit an equivalent circuit that can quantify an electrochemical system [22]. The full equation for a general system is defined as

$$Z(\omega) = Z_0 \cos(\emptyset) + Z_0 \sin(\emptyset)\, j$$
$$Z'_{real} = Z_0 \cos(\emptyset)\text{: } \textit{R(resistance)}$$
$$Z''_{img} = Z_0 \sin(\emptyset)\text{: } \textit{C(capacitance) + L(inductance)}$$

Nyquist plots graph real versus negative imaginary Z" impedance in Cartesian coordinates as it sweeps AC frequencies. The resistance of the system is the diameter of the semicircle formed from the plot at its high frequencies. This semicircle's diameter can be analyzed as the resistance of the electrolyte.

A common cell model used for EIS is the Randles cell model. It fits the data of a Nyquist plots into an equivalent circuit. The semicircle of the Nyquist plot is denoted by the parallel R_1 and C_1 parts, and R_2 is the offset of the semicircle region from the origin. It includes the Warburg impedance, indicated by the 45º angle to the right of the semicircle and included into equivalent

circuit in series with R_1 and in parallel with C_1. The Warburg impedance is associated with the slow transport process of chemical Li diffusion [22].

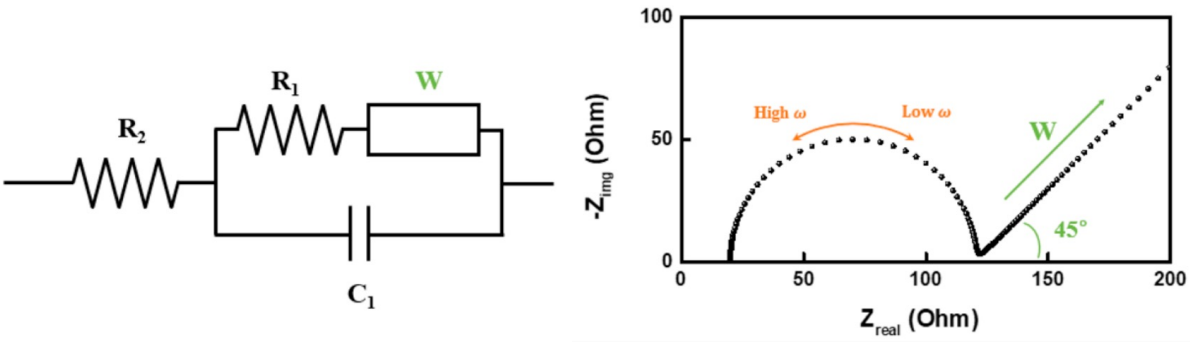

Figure 4.1: Equivalent circuit and Nyquist plot of a Randles cell model.

An ideal graph for calculating the Warburg impedance has a 45-degree angle relative to the x axis in the Nyquist plot; this slope is the Warburg coefficient σ. To find the Warburg impedance the equation below can be used:

$$D_{Li+} = \frac{1}{2}\left[\left(\frac{V_M}{SF\sigma}\right)x\left(\frac{\partial E}{\partial x}\right)\right]^2$$

in which V_M is the molar volume of active material, F is the Faraday constant (96,486 C/mol), S is the electrode/electrolyte contact area, σ is the Warburg coefficient, and $\partial E/\partial x$ is the slope of the charge and discharge curves [22]. It is only viable for solid-solution (i.e., the single-phase region) behavior, so other methods that take into account more than just the single-phase region obtain higher diffusion coefficients than data collected from EIS measurements [23]. These other methods include Li-ion transport within grain boundaries.

With the resistance information from the Nyquist plots, resistivity can be calculated using the equation

$$\rho = \frac{RA}{l}$$

in which ρ = resistivity, R = resistance, A = cross-sectional area, and l = length of sample.

To find the conductivity and activation energy, the resistivity value can be used. Conductivity is simply the inverse of the resistivity, and the activation energy is calculated by using the Arrhenius equation

$$\sigma = Aexp\left(-\frac{E_a}{kT}\right)$$

in which σ = conductivity [S/cm], E_a = activation energy (eV), k = Boltzmann's constant, and T = temperature (K). A can be calculated by plotting the slope of a ln(σ) vs 1/T graph, and then

$$E_a = k * slope$$ [24].

4b. Impedance Measurement Test Procedure

After the overnight oven bake from the synthesis process, the plastic tube containing the gel sample was opened at both ends, and two stainless steel contacts were inserted at each end of the tube. Some ILE was inserted to provide good contact, and a small hole was poked in the plastic tube to release any air bubbles. The setup was then placed in an oven connected to an impedance channel using stainless steel clamps. A probe to measure temperature was close to the sample to procure a more accurate temperature reading. Using EC Lab, the impedance was measured at 15 ºC intervals between 20 ºC and 80 ºC using electrochemical impedance spectroscopy (EIS). Any temperature past 80 ºC caused the plastic part to warp and rendered the samples unusable. The frequency range for EIS was from 1 MHz to 100 mHz with a 10 mV amplitude. The temperature in the oven was allowed to stabilize for about half an hour before taking the measurement, and the temperature was verified by a thermocouple placed close to the sample.

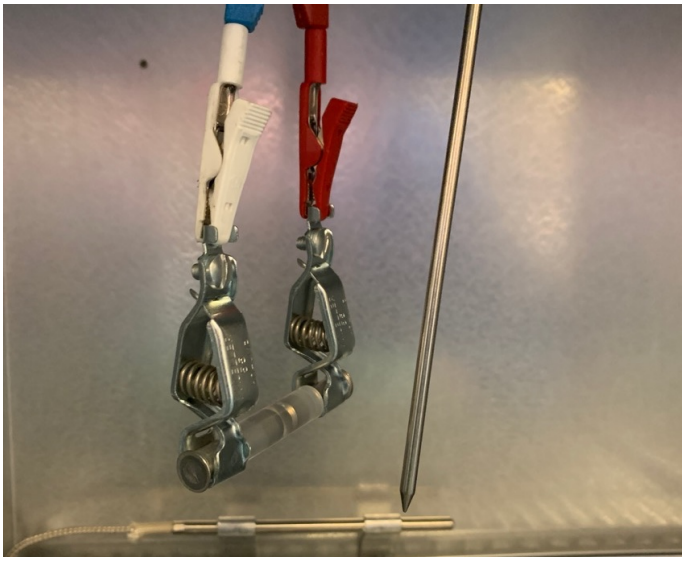

Figure 4.2: Setup of impedance test samples.

It was noted that the samples needed to be adjusted once they reached higher temperatures. At 65 ºC, the resistance went up, which defies expectations for decreased resistance at higher temperatures. This trend continued at 80 ºC. It was discovered that the plastic tube containing the sample and the metal contacts expanded a little, creating air pockets that reduced the integrity of the metal contacts. To remedy this issue, the contacts were carefully pressed inwards to improve the contact with the sample. As shown in Figure 4.3, the resistance shows its expected trend once this contact integrity is tested. For reference, the difference in actual resistance values in the figure is due to different samples shown and is not because of this modification.

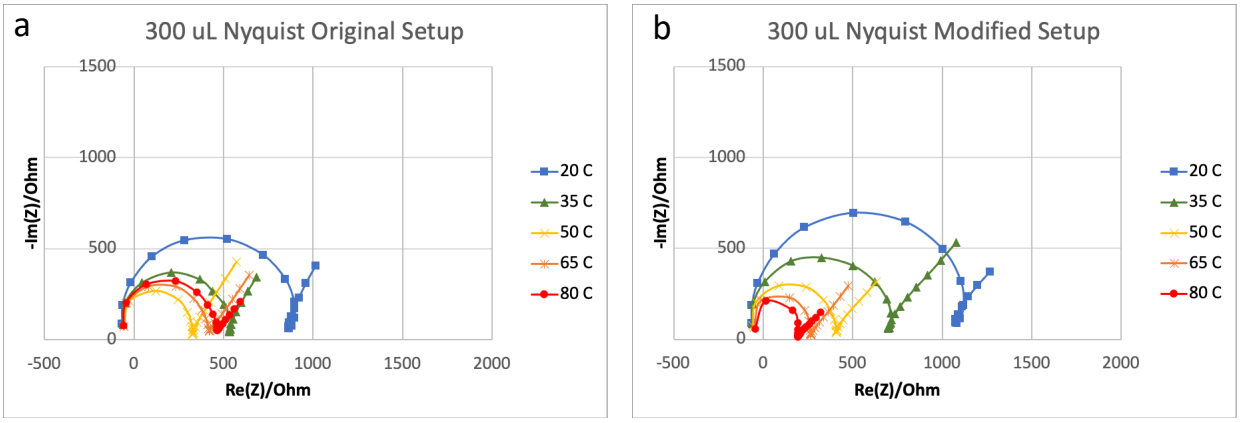

Figure 4.3: Impedance comparison before and after setup modification.

4c. Results and Analysis

Changing the amount of ILE in the fabricated sol-gels is likely to change the performance of the samples. It is anticipated that increasing the amount of ILE in the gel will increase the conductivity. The supporting evidence behind this hypothesis is the increase in amount of available Li salt and the increase in the average pore size. More available Li salt will increase the number of carriers while increasing pore size will allow for easier conduction of Li+ ions through the sol-gel network. Therefore, in order of increasing conductivity, the samples are expected to be 250 µL, 300 µL, then 350 µL.

Representative data for the ionogels is below. Figure 4.4 shows the raw data that is collected from EIS. The semicircle is the main focus, as its diameter is what determines the resistance. However, some of the tail is shown, from which the Warburg coefficient can be calculated.

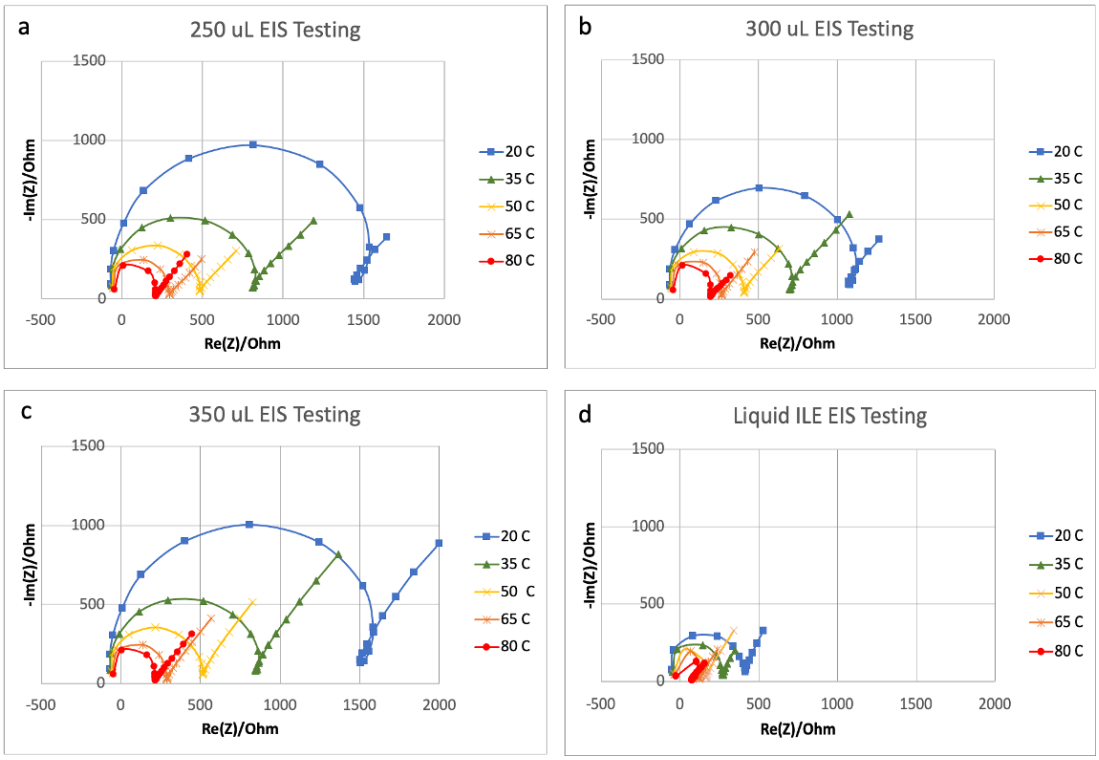

Figure 4.4: Representative impedance data for all samples and ILE reference.

For reference, the pure ILE was measured using EIS as well. Its resistance is much lower in part because the length of the sample tested was smaller than the ionogel samples. This will be taken into account when calculating resistivity.

The slope of the tail is the Warburg coefficient, and the values from the graphs above are in the table below.

Table 4.1: Warburg Coefficients for Impedance Data as a Function of Temperature

Temperature (ºC)	250 µL	300 µL	350 µL	ILE
20	1.138	1.126	1.219	2.095
35	1.067	1.254	1.260	1.877
50	1.064	1.146	1.308	1.629
65	1.092	1.256	1.279	1.481
80	1.310	0.999	1.221	1.205
Avg. Deviance from Ideal Value (1)	0.134	0.157	0.257	0.657

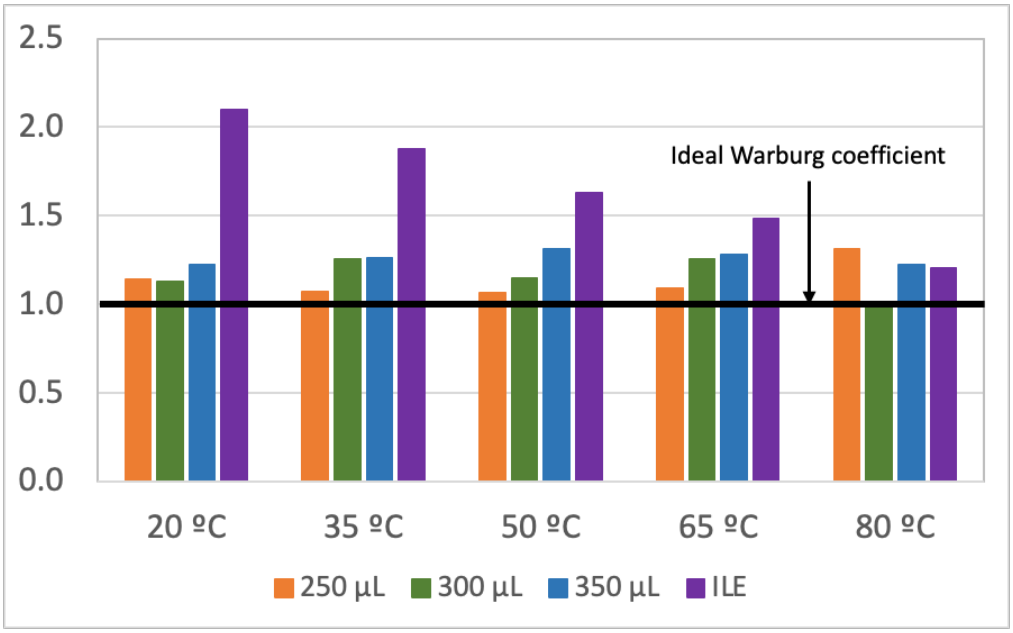

Figure 4.5: Warburg coefficients for all samples at 5 different temperatures.

The Warburg coefficients from the representative data are close to 1. This is the ideal value, since the tail of the EIS graph should be 45º from the x axis. This data is in good agreement with

the ideal equivalent circuit for electrolyte and indicates the bulk diffusion of the Li+ ions. Interestingly, the coefficient increases away from 1 with increased ILE. This could be due to other diffusion effects occurring with more ions, rather than just bulk diffusion through the samples [23]. EIS is still an accurate method for these ionogels because they are homogeneous and single-phase.

From the Nyquist plots, the conductivity and activation energy can also be calculated. This data is in Figure 4.6.

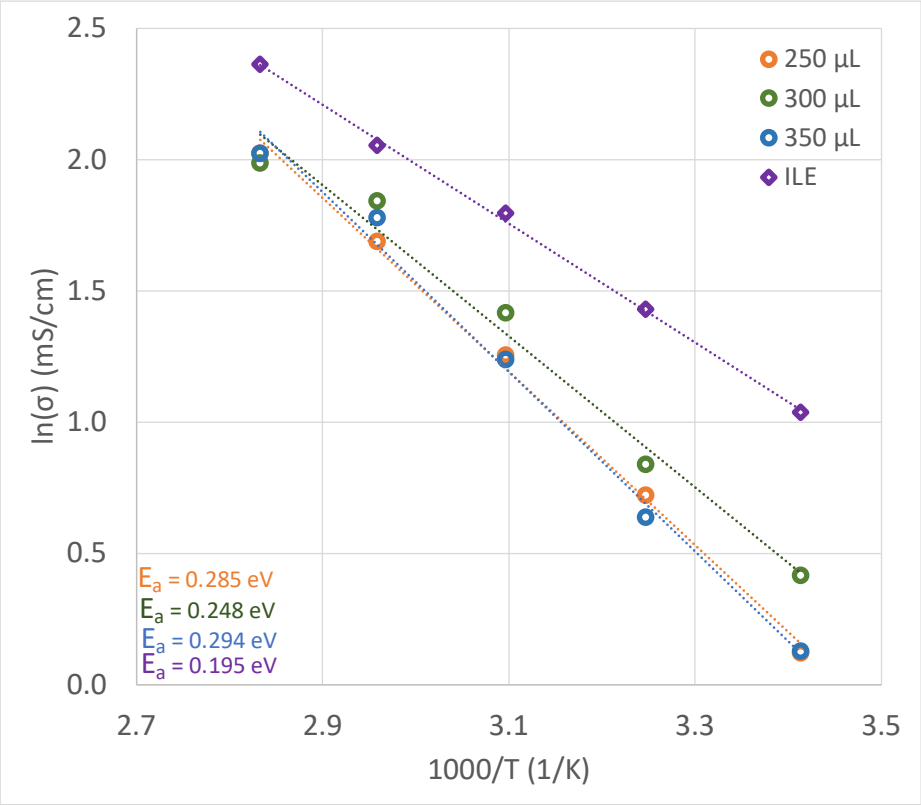

Figure 4.6: Arrhenius plot for conductivity temperature dependence for all three sample types and ILE reference.

The data collected for conductivity and activation energy does not fully support the hypothesis previously made. The conductivity increases from the 250 µL sample to the 300 µL sample, but it decreases back to the 250 µL range for the 350 µL sample. A property not taken into account in the hypothesis is that the higher ILE content leads to a higher viscosity of the material. From this, it could be more difficult for diffusion to occur through the sample despite the higher

amount of Li+ ions. Because of this, the 350 µL sample had more salt and diffusive material, but the increased viscosity could have decreased the conductivity. Conversely, the 250 µL sample had less salt but was less viscous due to smaller proportional ILE content. From this data, it sems that the 300 µL sample hit the "sweet spot" of ion content and viscosity for the highest conductivity of the ionogel samples.

A solution to this issue, given these results, could be to use less ILE but increase the molar fraction of Li salt in the electrolyte. If the concentration of salt is too high, the conductivity actually decreases due to the strong interactions between the lithium ions and the $[TFSI]^-$ structures [25]. These strong reactions increase viscosity quicker than other ionic liquids like $[FSI]^-$ types and change the coordination from bidentate to monodentate. This switch to monodentate coordination reduces the binding sites from two to one, which lowers the system's capability to diffuse ions [25]. J. Tong. et al. also concluded that 0.5 M has the highest self-diffusion coefficient between 0.3 and 2.0 M, so increasing the salt concentration will not increase the conductivity as proposed above [25].

The activation energies of the respective samples also match the conductivity trends. The lower the activation energy the easier it is for a species to be transported, and this is the case for the ILE with the lowest activation energy of 0.195 eV. The 300 µL sample follows at 0.248 eV, and the 250 µL and 350 µL samples are very similar at 0.285 and 0.294 eV respectively. This matches the conductivity trends in the Arrhenius plot and is in the same range as previous work [13][26].

The data collected shows a slight reduction in conductivity but is fairly close to the pure ILE conductivity. This is likely due to tortuosity effects, in which the pores create winding pathways that impede some of the ion transport in the sample. This is also consistent with previous

results on these types of gels [13]. Regardless, the results here are indicative that conductivity is not that much different between the ionogels and the pure ILE, especially at higher temperatures. At higher temperatures the conductivities of the ionogels themselves become more similar, indicating that temperature-dependent diffusion outweighs any contributions from viscosity or Li salt amount at these temperatures. The ionogels in this experiment mostly live up to the expectations for conductivity performance; while they are not as conductive as the pure ILE, the trade-offs for safter battery materials may be worth it for specific applications.

Table 4.2: Conductivity of Representative Impedance Data

Temperature (ºC)	250 µL (mS/cm)	300 µL (mS/cm)	350 µL (mS/cm)	ILE neat (mS/cm)
20	1.13	1.51	1.13	2.82
35	2.06	2.31	1.89	4.18
50	3.51	4.12	3.44	6.02
65	5.41	6.31	5.92	7.80
80	7.57	7.28	7.57	10.6

5. Microstructure Data and Analysis

5a. Microstructure Analysis Background

The Brunauer-Emmett-Teller method, or BET, is the most-used procedure for analyzing the pore surface area of porous materials [27]. It is used to calculate physisorption isotherms for adsorbed and desorbed molecules in a sample. For reference, adsorption is the enrichment of molecules, atoms, or ions within the relative space of an interface, while absorption is when molecules penetrate the surface and enter the bulk of the solid [27]. And specifically, physisorption (physical adsorption) is purely a physical phenomenon in which van der Waals attractions are the cause of adsorption. Adsorption isotherms are the relation between amount adsorbed and the equilibrium pressure of the gas at a constant temperature. The pressure at which the isotherm is at its maximum adsorbed volume is the saturation pressure p°. In practice the constant temperature

is the boiling point of the adsorbate gas. Nitrogen, which has a boiling point of 77 K, is normally used as the gas adsorbate because it is readily available, inert, and adsorbs easily with most solids. During physisorption, three stages occur in all but the smallest pores. In monolayer adsorption, all adsorbed molecules are in contact with the adsorbent surface. In multilayer adsorption, there are multiple adsorbed molecular layers, so not all molecules are in contact with the surface. And finally, pore condensation refers to the condensation of the gas into a liquid-like phase when the pore is at a pressure less than the saturation pressure of the bulk liquid [27].

BET is an extension of the Langmuir theory that applies kinetics of the adsorption process to multiple layers [28]. The derivation in its method yields an equation for the isotherm in linear form as

$$\frac{p/p^\circ}{\boldsymbol{n}(1-p/p^\circ)} = \frac{1}{\boldsymbol{n}_m C} + \frac{C-1}{\boldsymbol{n}_m C}(p/p^\circ)$$

in which $\mathbf{n}$ is the specific amount adsorbed at the relative pressure p/p° and $\mathbf{n}_m$ is the specific monolayer capacity. The constant C is related to the energy of monolayer adsorption [27]. The left side of the equation, when plotted against p/p°, should give a straight line that has an intercept of $1/\mathbf{n}_m C$ and a slope of $(C-1)/\boldsymbol{n}_m C$. From this graph C and $\mathbf{n}_m$ can be calculated [28]. With extra sample knowledge, the BET-area using the specific monolayer capacity can be calculated as

$$a_s(BET) = \boldsymbol{n}_m L \sigma_m / m$$

in which a_s(BET) is the BET specific area of the adsorbent (of mass m), L is Avogadro's constant, and σ_m is the molecular cross-sectional area [27].

The isotherms using this method are S-shaped and have varying characteristics based on the sample system. Hysteresis can occur for many reasons, including pore condensation, metastability in open-ended pores that prevent the system from being in thermodynamic

equilibrium, and complex networks that block desorption like wide pores only accessible through narrow necks [27].

While knowing the surface area of the porous aerogels is important, the pore size and size distribution is useful as well. The Barrett-Joyner-Halenda method, or BJH, has been widely used to determine this information using BET measurement methods. The method uses two assumptions: the pores are cylindrical and the adsorbed amount results from physical adsorption as well as capillary condensation. The method is best used on mesopores, which are nanopores with a 2-50 nm width [29]. The method yields the equation

$$\ln\left(\frac{p}{p^0}\right) = \frac{2\gamma V_M}{rRT}$$

in which γ is the surface tension of the adsorbate in liquid form, V_M is the molar volume of the liquid, r is the radius of the meniscus found in the mesopore, R is the universal gas constant, and T is the temperature. This equation calculates the change in thickness of adsorbed film from the decrease of relative pressure in the desorption curve [30]. This change is meant to represent the evacuation of capillary condensate and the thinning of the physically adsorbed film. However, this method cannot accurately measure pore thickness in macropores (widths > 50 nm) because its assumptions do not account for physical effects like tensile strength or pore network effects [30].

5b. Microstructure Test Procedure

The microstructure samples were created via the synthesis process in Materials and Methods, but they needed further processing before they could be measured. The sol-gels must be converted to aerogels, which are the gels when all liquids have been removed while still preserving their structure. It is important to successfully create aerogels so the true microstructure of the sol-gels can be observed.

The ionogels, once they finished the heating step in the oven to remove any remaining solvents, were placed in acetone for solvent exchanges. The ILE is miscible with acetone, so the acetone gradually replaced the ILE trapped in the silica matrix. Several solvent exchanges were performed, and the vials were placed on a shaker table to agitate the samples and encourage solvent replacement. This normally lasted 5-7 days. Removal of the acetone was performed by supercritically drying the samples. The samples were placed inside a pressure chamber that pumped in liquid CO_2 and drained out the acetone i.e., another solvent exchange. This was performed until the CO_2 replaced all the acetone, and then the system was brought to the supercritical point of CO_2, which is 1070 psi at 31 ºC [31]. At this point, the CO_2 became a supercritical fluid and escaped the pores without collapsing the structure. After the supercritical CO_2 escaped the samples, the chamber was slowly vented and temperature reduced until the samples were back at ambient conditions. Prior to analysis, the samples were once again put in an oven to remove any water adsorbed from the atmosphere.

In the microstructure analysis, the sample was placed into a testing fixture (normally called a cell) and is degassed to remove adsorbed water and volatiles that it accumulated during storage [30]. The testing was performed using a Micromeritics ASAP 2020 Plus instrument. Nitrogen, the adsorbate gas used, was incrementally added into the cell at its boiling temperature of 77 K. Adsorption is calculated by the difference between the measured pressure and the pressure of the empty cell; this correlates with the moles of adsorbed gas.

5c. Results and Analysis

It is hypothesized that the amount of ionic liquid would affect the porosity and pore size of the aerogels. The silica precursors, when their ratios are more or less than the standard formulation, will likely make it easier and harder, respectively, to form the network. Less ILE (and more silica)

could yield a tighter-knit, more interconnected structure. This would likely reduce the pore size and increase the porosity. More ILE (and less silica) could yield a more open, less connected structure. This would likely increase the pore size and decrease the porosity. It is likely that a more open structure will increase conductivity but the structure itself will be weaker and more prone to damage. So, the 250 µL sample is expected to have the smallest pore size and the 350 µL sample will have the largest pore size.

The first set of BET and BJH data was performed to confirm that the process used for later work was accurate. Using the synthesis by Néouze et al. described in Methods and Materials, BET data was collected to compare with the graphs in the paper.

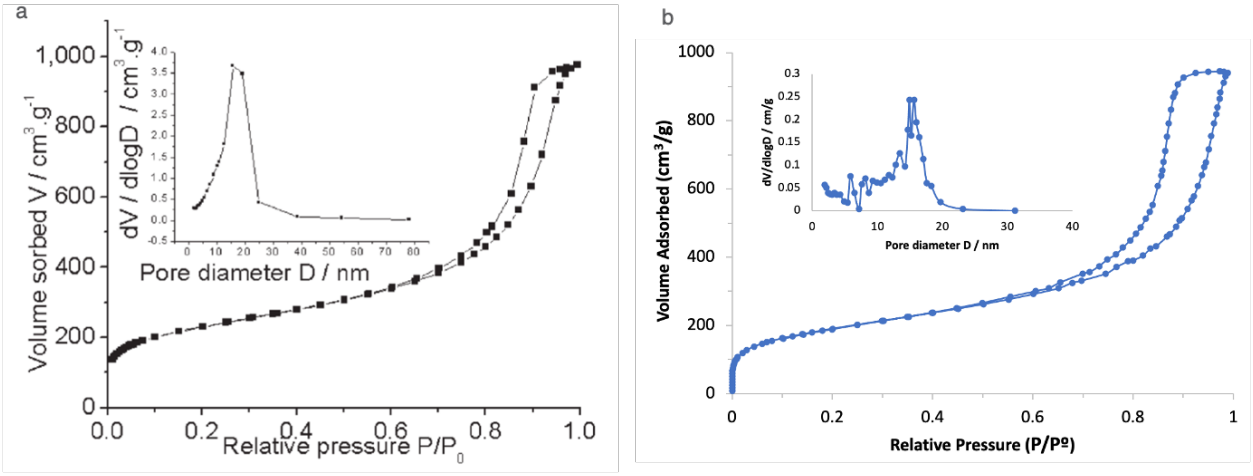

Figure 5.1: Isotherms and pore distributions for Néouze reference and current results.

The data collected shows accurate comparison to the previous work, with similar adsorption curve maximums around 1000 cm^3/g and the same pore distribution peak at around 18 nm. The only significant difference is that the derivative value for the current work is lower than that of the reference distribution, indicating that the pore sizes are more uniform and do not change drastically. There is also a greater hysteresis in the current work than the reference, suggesting that capillary condensation was more prevalent in the current work [27]. It must be noted that the Néouze paper uses the desorption curve for its BJH analysis, which is not normally used to

determine pore size. This is because desorption can be different from adsorption if there is a type of pore morphology that will prevent equivalent desorption e.g., pores with narrow necks and larger cavities [27]. Thus, it may not accurately represent the actual characteristics of the porous sample. Regardless, the data for the current work used the desorption curve to match the reference data.

While the Néouze data was very similar to the previously stated work, this was not the case for the gels that were modified from the Ashby formulation. The reference data could not be replicated, even though the process for creating ionogels was viable as supported by the Néouze recreation.

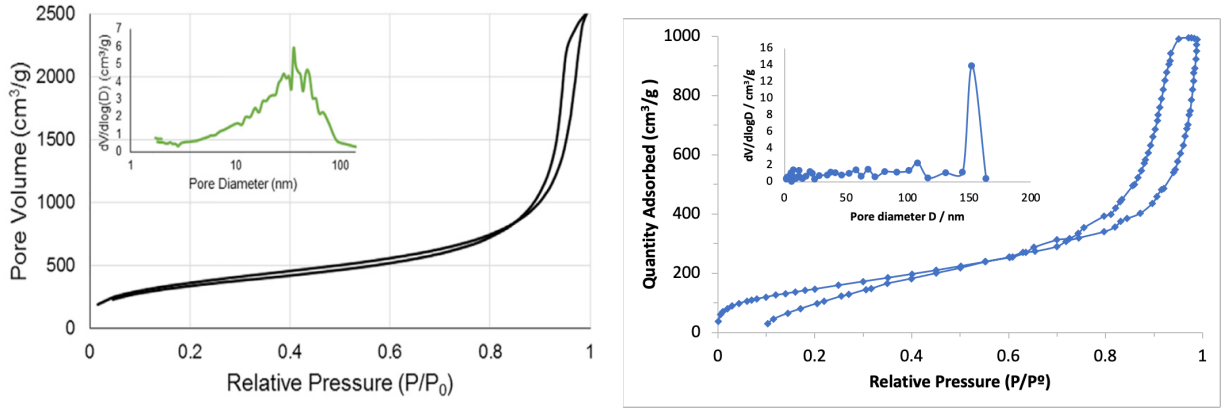

Figure 5.2: Reference data from Ashby and best isotherm and pore size distribution for current results.

There are quite a few differences between the reference data and the collected results. The lower maximum value for the new data shows that the sample did not adsorb as much nitrogen as previously documented. This indicates that there is a lower surface area in the new sample and therefore has larger pores. The surface area was calculated to be 551 m^2/g compared to the previously reported 1300 m^2/g, so this data is consistent with the isotherm. The hysteresis in the desorption branch is not ideal, especially in crossing the adsorption curve at 0.5 relative pressure

and the curve ending around 0.1. Such a large hysteresis and the desorption branch crossing the adsorption branch is a sign that the machine is heating up and the temperature during the test is not always at 77 K, the boiling point of nitrogen. Operating the test at a nonideal temperature prevents adsorption changes from being accurately measured. This did not occur on another machine, supporting the evidence that this is a machine issue. The BJH pore size distribution graph, inset in the isotherm graph, is also not ideal. The peak at 150 nm cannot be fully trusted, since BJH is known to be inaccurate for any pore size over 50 nm. Because there is no peak within the detectable width range, this does corroborate the conclusion from the isotherm peak. The pore size is in the macropore range and is much larger than the ~20 nm size in the reference data. Therefore, the microstructure data collected was not able to support the hypothesis for pore size characterization.

Though it was not possible to find the average pore size of the samples, the microstructure does not appear to have had a large effect on the conductivity. Though the 300 µL sample has slightly higher conductivity than the 250 µL and 350 µL samples, they are still very close together and noticeably less than neat ILE in Figure 4.6. This would indicate that microstructure is not significantly affecting the performance of the ionogel. The conductivities are similar to the previous work, so even between sample sets the microstructure is not significantly important.

6. Conclusion

Ionogels have become an emerging interest in the research community due to increased demand for batteries in all parts of life. As energy demand increases, more energy-dense batteries that can operate safely are needed. Solid electrolytes, particularly ionogels, are good candidates for these systems because their solid structure is such that the trapped liquid electrolyte can still behave as a liquid at the nanoscale. In this study, the amount of ILE was varied during synthesis

in order to observe the conductivity at different temperatures and the resultant microstructures. The conductivities of the ionogel samples at room temperature were 1.13 mS/cm for the 250 and 350 µL samples and 1.51 mS/cm for the 300 µL sample; these values are half of the neat ILE conductivity at 2.82 mS/cm. This gap was reduced at the highest tested temperature of 80 ºC, as they were all similar values and were 70 percent of the ILE value of 10.6 mS/cm. The activation energies were also fairly close to the neat ILE value (0.285 for 250 µL, 0.248 for 300 µL, and 0.294 eV for 350 µL to 0.195 eV) and were consistent with literature. This similarity to the liquid ILE suggests that the porous structure worked well to provide liquid behavior for conductivity. There was not a significant difference between the 250 µL, 300 µL, and 350 µL samples, but the original synthesis (300 µL) had the highest conductivity and lowest activation energy overall. The microstructure data was less helpful, as the pores were too large to be captured by the available detection method. This study furthers the research into ionogels' capabilities as solid-state electrolytes and shows promising trends for a larger-scale adoption into commercial batteries.

7. Future Work

There are a couple of pathways to improve upon the results shown in this work. Creating a sturdier test fixture to test the impedance at higher and lower temperatures could be beneficial for observing trends on a larger scale. Because solid state electrolytes are desired for their prevention of dendrite formation, these ionogels can be integrated into battery systems and compared with a standard liquid electrolyte to assess their influence. Also, the conductivity trends might be different as interactions with the electrodes might initiate other reactions not present in a solo electrolyte test.

There is a lot more work that can be done with the microstructure data to come to a more satisfying conclusion. Failure analysis can be performed to discover why the average pore size was

consistently so much higher with this replication of previous work. With a lower average pore size, it is easier to analyze the distribution due to the limitations of the BJH method. Then, the difference between the different sample types might be more apparent.

References

[1] Ding, Y. et al. (2019). Automotive Li-Ion Batteries: Current Status and Future Perspectives. *Electrochem. Energ. Rev.* 2, 1-28.

[2] Roy, P. et al. (2015). Nanostructured anode materials for lithium ion batteries. *J. Mat. Chem. A.* 3, 2454-2484.

[3] Balasubramaniam, B. et al. (2020). Recycling of Lithium from Li-ion Batteries. *Enc. Renewable and Sust. Mat.* 2, 546-554.

[4] Winter. M., and Brodd. R.J. (2004). What are Batteries, Fuel Cells, and Supercapacitors? *Chem. Rev.* 104, 4245-4269.

[5] Goodenough, J. B. and Kim, Y. (2010). Challenges for Rechargeable Li Batteries. *Chem. Mater.* 22, 587-603.

[6] Nitta, N. et al. (2015). Li-ion battery materials: present and future. *Mater. Today.* 18(5), 252–264.

[7] Zhang, J.G. et al. (2012). Silicon-Based Anodes for Li-ion Batteries. *Enc of Sust. Sci. and Tech.* 9293-9316.

[8] Li, M. et al. (2020). New Concepts in Electrolytes. *Chem. Rev*. 120, 6783−6819.

[9] Li, Q. et al. (2016). Progress in electrolytes for rechargeable Li-based batteries and beyond. *Green Eng. and Env.* 18-42.

[10] Xu. K. (2004). Electrolytes for Lithium-Based Rechargeable Batteries. *Chem. Rev.* 104(10), 4303-4417.

[11] Manthiram, A., Yu, X. and Wang, S. (2017). Lithium battery chemistries enabled by solid-state electrolytes. *Nat. Rev. Mater*. 2, 1–16.

[12] Hyun, W.J., Thomas, C.M., and Hersam, M.C. (2020). Nanocomposite Ionogel Electrolytes for Solid-State Rechargeable Batteries. *Adv. Energy Mater.* 10, 2002135.

[13] Ashby. D.S. et al. (2017). Patternable, Solution-Processed Ionogels for Thin-Film Lithium-Ion Electrolytes. *Joule*. 1, 1-15.

[14] Vioux, A. et al. (2010). Use of ionic liquids in sol-gel; ionogels and applications. *C. R. Chimie*. 13, 242-255.

[15] Galiński, M., Lewandowski, A., and Stepniak, I. (2006). Ionic liquids as electrolytes. *Electrochim. Acta.* 51, 5567–5580.

[16] Schubert, U. (2015). 1: Chemistry and Fundamentals of the Sol-Gel Process. *Wiley-VCH.* 1-28.

[17] Adnan, M, et. al. (2018). *in situ* Synthesis of Hybrid Inorganic-Polymer Nanocomposites. *Polymers*. 10. 1129.

[18] Innocenzi, P. (2019). The Sol-to-Gel Transition. *Springer, Cham.* 2nd edn.

[19] Li, L., Li, S., and Lu, Y. (2018). Suppression of dendritic lithium growth in lithium metal-based batteries. *Chem Commun*. 54(50), 6648–6661.

[20] Tarascon, J.M. and Armand, M. (2001). Issues and challenges facing rechargeable lithium batteries. *Nature.* 414, 359–367.

[21] Néouze, M-A. et al. (2005). A route to heat resistance solid membranes with performances of liquid electrolytes. *Chem Commun.* 1082-1084.

[22] Choi, W. et. al. (2020). Modeling and Applications of Electrochemical Impedance Spectroscopy (EIS) for Lithium-ion Batteries. *J. Electrochem. Sci. Technol.* 11(1), 1-13.

[23] Rui, X.H. et al. (2010). Analysis of the chemical diffusion coefficient of lithium ions in $Li_3V_2(PO_4)_3$ cathode material. *Electrochim. Acta.* 55, 2384-2390.

[24] Sudha L. K., Roy, S., and Rao, K.U. (2014). Evaluation of Activation Energy (Ea) Profiles of Nanostructured Alumina Polycarbonate Composite Insulation Materials. *Int. J. Materials, Mech. and Manuf.* 2(1), 96-100.

[25] Tong, J. et al. (2020). The Effect of Concentration of Lithium Salt on the Structural and Transport Properties of Ionic Liquid-Based Electrolytes. Front. Chem. 7(945), 1-10.

[26] Tan, G. et al. (2016). Solid-state Li-ion batteries using fast, stable, glassy nanocomposite electrolytes for good safety and long cycle-life. *Nano Lett*. 16, 1960–1968.

[27] Thommes, M. (2015). Physisorption of gases (2015). *Pure Appl. Chem*. 87(9-10): 1051-1069.

[28] Brunauer, S., Emmett, P.H., and Teller, E. (1938). Adsorption of Gases in Multimolecular Layers. *J. Am. Chem. Soc.* 60, 309-319.

[29] Barrett, E.P., Joyner, L.G., and Halenda, P.P. (1951). The Determination of Pore Volume and Area Distributions in Porous Substances. *J. Am. Chem. Soc*. 73, 373-380.

[30] Bardestani, R., Patience, G.S., and Kaliaguine, S. (2019). Experimental methods in chemical engineering: specific surface area and pore size distribution measurements—BET, BJH, and DFT. *Can J Chem Eng*. 97, 2781–2791.

[31] Span, R. and Wagner, W. (1996). A New Equation of State for Carbon Dioxide Covering the Fluid Region from the Triple-Point Temperature to 1100 K at Pressures up to 800 MPa. *J. of Phys. Chem. Ref. Data*. 25(6), 1509–1596.